Mon. Not. R. Astron. Soc. **000**, 000–000 (0000) Printed 30 July 2019 (MN LATEX style file v2.2)

The 2018 eruption and long term evolution of the new high-mass Herbig Ae/Be object Gaia-18azl = VES 263

U. Munari[1], V. Joshi[2], D.P.K. Banerjee[2], K. Čotar[3], Shugarov S.Y.[4], R. Jurdana-Šepić[5], R. Belligoli[6], A. Bergamini[6], M. Graziani[6], G.L. Righetti[6], A. Vagnozzi[6], P. Valisa[6]

[1] *INAF Astronomical Observatory of Padova, 36012 Asiago (VI), Italy*
[2] *Physical Research Laboratory, Navrangpura, Ahmedabad, Gujarat 380009, India*
[3] *Faculty of Mathematics and Physics, University of Ljubljana, Jadranska 19, 1000 Ljubljana, Slovenia*
[4] *Sternberg Astronomical Institute, M.V. Lomonosov Moscow State University, Moscow 119991, Russia*
[5] *University of Rijeka, Physics Department, Radmile Matejčić, 51000, Rijeka, Croatia*
[6] *ANS Collaboration, Astronomical Observatory, 36012 Asiago (VI), Italy*

30 July 2019

ABSTRACT

We have been monitoring, at high cadence, the photometric and spectroscopic evolution of VES 263 following the discovery in 2018 of a brightening labeled as event Gaia-18azl. VES 263 is so far a neglected emission-line object discovered in the 1960s on objective prism plates, tentatively classified as a semi-regular AGB cool giant by automated analysis of ASASSN lightcurves. We have discovered that VES 263 is a bonafide massive pre-Main Sequence object ($\sim$12 $M_\odot$), of the Herbig AeBe type. It is located at 1.68$\pm$0.07 kpc distance, within the Cyg OB2 star-forming region, and it is highly reddened (E_{B-V}=1.80$\pm$0.05) by interstellar extinction. In quiescence, the spectral energy distribution is dominated by the $\sim$20,000 K photospheric emission from the central B1II star, and at $\lambda \geqslant 6\mu$m by emission from circumstellar warm dust ($T \leqslant 400$°K). The 2018-19 eruption was caused by a marked brightening of the accretion disk around the B1II star as traced by the evolution with time of the integrated flux and the double-peaked profile of emission lines. At the peak of the eruption, the disk has a bulk temperature of $\sim$7500 K and a luminosity $L \geqslant 860$ $L_\odot$, corresponding to a mass accretion rate $\geqslant 1.1\times10^{-5}$ $M_\odot$ yr^{-1}. Spectroscopic signature of possible bipolar jets (at -700 and $+700$ km s^{-1}) of variable intensity are found. We have reconstructed from Harvard, Moscow and Sonneberg photographic plates the photometric history of VES 263 from 1896 to 1995.

Key words: stars: pre-main-sequence; stars: variables: T Tauri, Herbig Ae/Be; open clusters and associations: individual: Cyg OB2

1 INTRODUCTION

On April 18, 2018 the Gaia team issued an alert for a 0.5 mag increase observed by Gaia on a field star located at (J2000) α=20^h 31^m 48^s.85, δ=+40° 38' 00".1, rising from a previous average of G=12.16 to G=11.66 mag. The brightening star was logged as Gaia-18azl, and the event was also filed as AT-2018awf by the IAU Transient Name Server. On this server, a couple of days past discovery, R. Fidrich noted the presence at this position of an anonymous star recognized as a variable by the ASASSN sky patrol (and logged as ASASSN-V J203148.85+403800.1). Fridrich commented as the ASASSN automated classification of the star as a semi-regular variable of P=197 days seemed unlikely given the ASASSN lightcurve, and suggested instead it being a young stellar object in outburst.

A positional search through the literature revealed Gaia-18azl being identical with VES 263, a poorly known emission-line star catalogued by the Vatican Emission Star survey (Wisniewski and Coyne 1976), and by Stephenson and Sanduleak (1977) as SS 447. The latter noted strong Hα in emission, but said nothing about the underlying continuum. The latter was classified as that of a B star by Downes and Keyes (1988) from spectroscopic observations but with no further details or a spectrum being shown. The

object was also observed as having the Hα line in emission in the course of the Hamburg Observatory objective-prism sky survey (carried out in 1964-70), entering the Kohoutek and Wehmeyer (1997, 1999) catalog as HBHα 4203-31. Comerón and Pasquali (2012, hereafter CP12), in the course of a survey of the Cygnus OB2 association and its surroundings in search for previously unrecognized massive stars, obtained a low resolution spectrum of the same object, logged as J20314885+4038001, without commenting on its positional coincidence with entries in catalogs of emission-line stars. They classified the spectrum as a highly reddened B1II star and in their plot, covering the range 3900-4900Å (i.e. Hϵ-Hβ), no emission line is readily evident, including Hβ that looks in normal absorption without an emission core.

VES 263 lies positionally close to the center of the massive Cygnus OB2 association, at the outskirts of the γ Cyg bright nebula and the dark cloud LDN 889 (Lynds 1962) which appears superimposed to it. Inspection of IRAS mid-IR maps shows VES 263 being at the very heart of a highly structured, knotty dust-complex extending for $\sim 2^\circ$ in radius. This is an area of intensive star formation, with the two highest mass Herbig Ae/Be stars lying close to VES 263 viz. MWC 1021 at 72 arcmin and V1478 Cyg at 14 arcmin. Herbig Ae/Be stars (HAeBes for short) are pre-main sequence stars of intermediate mass, spanning the range between the lower-mass T Tauri stars and the embedded massive young stellar objects (MYSOs). The most recent catalog of HAeBes by Vioque et al. (2018), lists 252 entries, with only 79 of them corresponding to B- or O-spectral types and the rest being cooler/lower-mass stars. The discovery of any new high-mass HAeBe object is therefore relevant given the limited number of such objects known in the whole Galaxy.

The B1II spectral type, the strong Hα feature in emission, the partnership with a site of ongoing stellar formation and the location at the boundaries of a dark interstellar cloud perfectly match VES 263 with the classification criteria formulated by Herbig (1960) for HAeBe objects. Motivated by this, after the Gaia alert we initiated a high cadence $BVR_{\rm C}I_{\rm C}$ monitoring, later augmented by low- and high-resolution optical spectroscopy, near-IR observations and a search through photographic archival repositories, the results of which are presented and discussed here. We will show how VES 263 is indeed a bona fide new HAeBe star, heavily obscured by interstellar extinction and with IR excess due to circumstellar dust, showing a complex century-long photometric history and a marked variability rapidly increasing toward the Infrared, in addition to a bright circumstellar disk where double-peaked emission lines form and which is responsible for the recorded photometric variability.

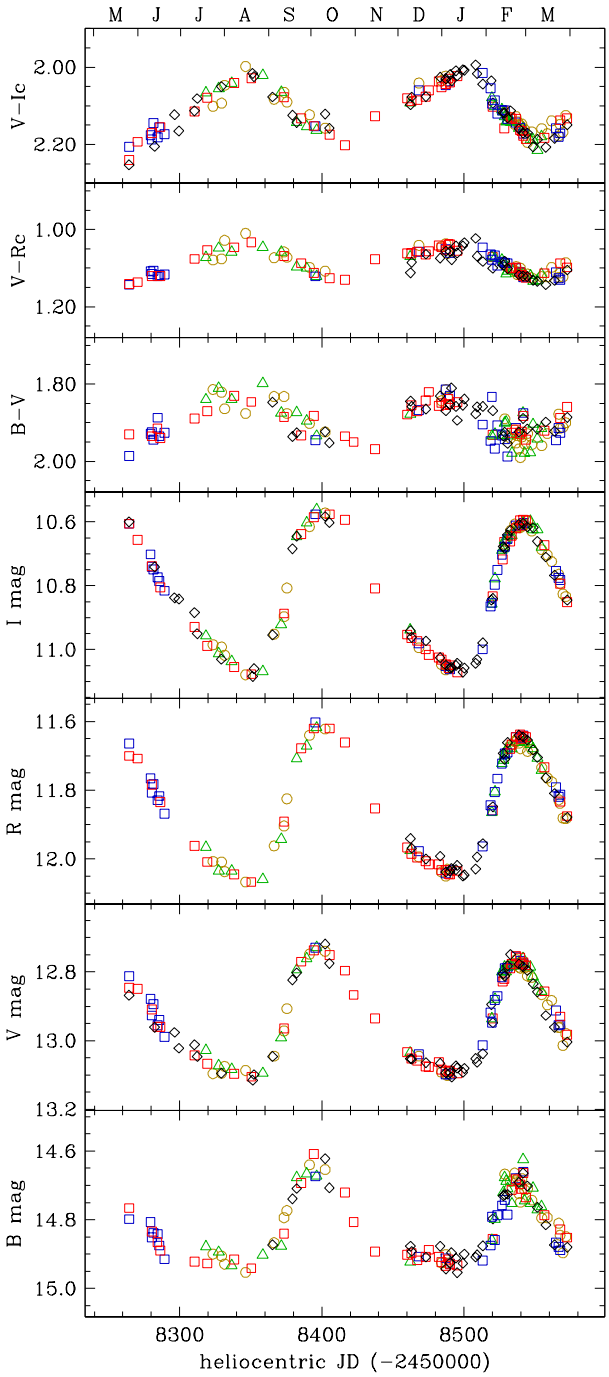

Figure 1. The $BVR_{\rm C}I_{\rm C}$ light- and color-evolution of the 2018-19 outburst of Gaia-18azl = VES 263 from our observations listed in Table 1. Data provided by different ANS Collaboration telescopes are marked with different symbols. Letters at the top mark the month from May 2018 to March 2019.

2 OBSERVATIONS

2.1 Optical photometry

$BVR_{\rm C}I_{\rm C}$ photometry (in the Landolt system) of VES 263 was obtained with five ANS Collaboration telescopes (with identifiers 606, 703, 1301, 1507, and 2900), all located in Italy and each working independently from all others (for simplicity, in the rest of the paper we will adopt R and I for band nomenclature instead of the more precise $R_{\rm C}$ and $I_{\rm C}$). The operation of ANS Collaboration telescopes is described in detail by Munari et al. (2012) and Munari & Moretti (2012). The observations at each site were transformed from the instantaneous local photometric system to the standard Landolt system via a common local photometric sequence established around VES 263 and covering a wide range in color that brackets that of the program star. An initial version of the local photometric sequence was extracted from the APASS all sky survey (e.g. Henden and Munari 2014)

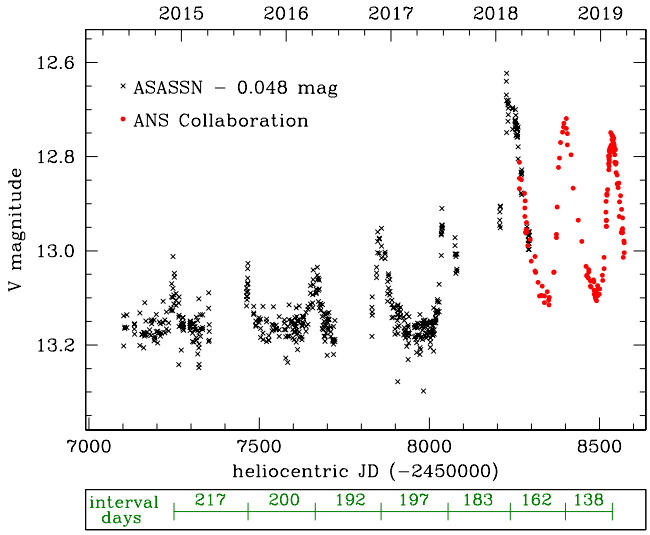

Figure 2. The recent photometric history of VES 263 constructed by combining archival V-filter photometry from the ASASSN project with current outburst V-band data from the ANS Collaboration. The latter are fully color transformed to the Landolt system, while ASASSN are not and require the indicated −0.048 mag shift to be brought into agreement with APASS and ANS photometry.

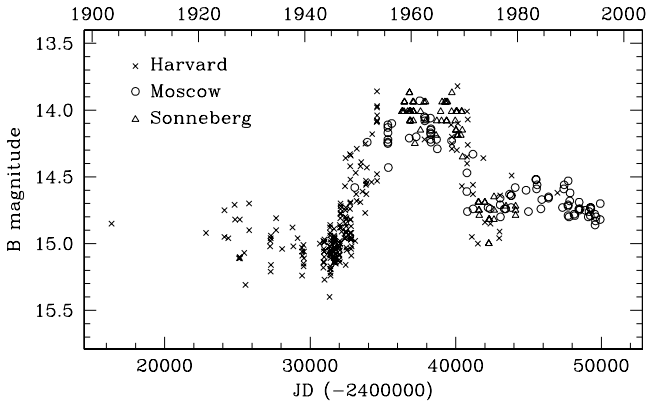

Figure 3. Historical blue-band lightcurve of VES 263 constructed from Harvard, Moscow and Sonneberg photographic plates.

and ported to Landolt equatorial system via the transformations calibrated in Munari et al. (2014). The sequence was then continuously improved as a by-product of the accumulating observations of VES 263, and by the end of the campaign, all observations were re-reduced on the central ANS Collaboration server against this improved and final sequence. In all we collected 163 independent $BVRI$ runs, on 109 different nights, from 2018 May 25 to 2019 March 30. The results are listed in Table 1 (available in full in electronic form only). The total error budget (quadratic sum of the Poissonian noise on the variable and the formal error on transformation from the local instantaneous system to the standard one via color equations) has a median value of 0.009 mag for the data in Table 1 and it is therefore omitted. The resulting color-and light-curves are plotted in Figure 1.

Table 1. Optical photometry of VES 263 (a small portion is shown here to provide guidance about its content: the full table is available in electronic form only). The last column lists the telescope identifier, the same as used in Figure 1.

HJD	B	V	R	I	ID
2458488.254	14.920	13.097	12.019	11.039	606
2458489.206	14.932	13.075	12.037	11.053	1507
2458490.211	14.938	13.076	12.035	11.046	1507
2458490.253	14.927	13.088	12.041	11.054	2900

2.2 Optical spectroscopy

Low, medium and high resolution spectra of VES 263 were obtained with three different telescopes located in Asiago and Varese (Italy). In all observations the spectrograph slit was aligned along the parallactic angle for optimal flux calibration, achieved by comparison against a spectrophotometric standard located close to VES 263 in the sky and observed either immediately before or after the target. Data reduction was carried out in IRAF and involved the usual steps on bias and dark removal, flat-fielding, variance-weighted spectrum tracing, sky subtraction, wavelength calibration, heliocentric correction and flux calibration. A log of the spectroscopic observations at optical wavelengths is provided in Table 2.

The Asiago 1.22m deployed a B&C spectrograph and ANDOR iDus DU440A camera housing a back-illuminated E2V 42-10 CCD (2048×512 array, 13.5 μm pixels). The low dispersion observations of VES 263 were obtained with a 300 ln/mm grating blazed at 5000 Å, providing a dispersion of 2.31 Å/pix over the range $\lambda\lambda$ 3300−8000 Å, while medium dispersion observations used two 1200 ln/mm gratings, one blazed at 4000 Å and the other at 6500 Å both giving a dispersion of 0.60 Å/pix.

On the Asiago 1.82m telescope, to record the high resolution spectra of VES 263, we used the REOSC-Echelle spectrograph, which is equipped with an EEV CCD47-10 CCD (1024×1024 array, 13 μm pixels). It covers the interval $\lambda\lambda$ 3700−7300 Å in 30 orders without inter-order gaps. A slit width of 1.5 arcsec was used resulting in a resolving power of 20,000.

The Varese 0.84m telescope was used in conjunction with a mk.III Multi Mode Spectrograph from Astrolight Instr., feeding light to a SBIG ST-10XME camera (2184×1472 array, 6.8 μm). The slit width was allowed to be variable between 2 and 3 arcsec in accordance with the seeing. In the Echelle configuration the Multi Mode Spectrograph covers the range $\lambda\lambda$ 4225−8910 Å in 27 orders, at a resolving power of 16,000 and without significant inter-order wavelength gaps. In the low dispersion mode, a 600 ln/mm grating blazed at 5000 Å was adopted allowing coverage of the interval $\lambda\lambda$ 4585−9490 Å at 2.10 Å/pix.

2.3 Near-IR

NIR spectroscopy and JHK_s band photometry of VES 263 were obtained at a few epochs with the 1.2m telescope of the Mount Abu Infrared Observatory (Banerjee &

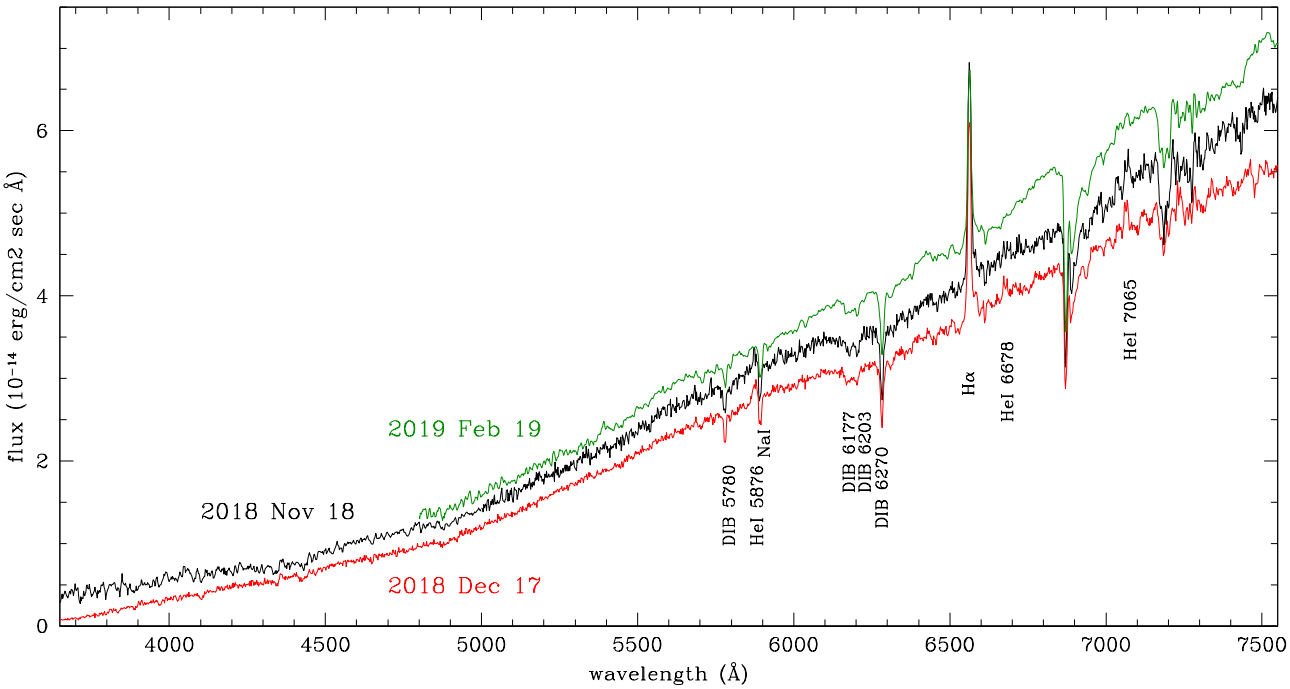

Figure 4. Sample low resolution spectra of VES 263 for three distinct states during the 2018-19 eruption: minimum (2018 Dec 17), peak (2019 Feb 19) and intermediate brightness (2018 Nov 18). The strongest interstellar absorption features and stellar emission lines are identified.

Table 2. Log of optical spectroscopy. The last column lists the integrated absolute flux of Hα (in units of 10^{-13} erg/cm^2 sec). The symbol ‡ marks nights without observations of spectrophotometric standard stars.

date	<UT> hh:mm	expt sec	disp. Å/pix	range Å	grating ln/mm	tel. ID	Hα (10^{-13})
2018 Jul 29	22:10	900	ECH	3700−7300		1.82m	2.845
2018 Nov 18	20:17	1200	2.31	3330−8025	300	1.22m	3.625
2018 Dec 11	18:45	5400	ECH	4225−8910		0.84m	2.924
2018 Dec 17	16:57	900	ECH	3700−7300		1.82m	‡
2018 Dec 17	17:29	1800	2.31	3210−7915	300	1.22m	3.080
2018 Dec 20	18:18	5400	ECH	4225−8910		0.84m	2.680
2018 Dec 21	17:02	3600	0.60	7360−8585	1200R	1.22m	
2018 Dec 22	18:00	3600	0.60	7635−8850	1200R	1.22m	
2018 Dec 24	17:14	3600	0.60	3810−5040	1200B	1.22m	
2018 Dec 26	17:32	3600	0.60	3810−5040	1200B	1.22m	
2018 Dec 27	17:44	7200	0.60	3780−5017	1200B	1.22m	
2018 Dec 27	18:09	3600	ECH	3700−7300		1.82m	‡
2018 Dec 29	17:55	5400	ECH	4225−8910		0.84m	2.618
2018 Dec 31	17:50	5400	ECH	4225−8910		0.84m	2.711
2019 Jan 02	18:00	5400	2.10	4585−9490	600	0.84m	2.785
2019 Jan 07	17:45	5400	2.10	4585−9490	600	0.84m	2.657
2019 Jan 25	17:27	2000	ECH	3700−7300		1.82m	2.502
2019 Feb 13	04:43	5400	2.10	4585−9490	600	0.84m	2.790
2019 Feb 16	03:49	3600	ECH	3700−7300		1.82m	3.090
2019 Feb 16	04:53	3600	2.10	4585−9490	600	0.84m	2.991
2019 Feb 17	04:05	3600	ECH	3700−7300		1.82m	3.021
2019 Feb 18	04:06	3600	ECH	3700−7300		1.82m	3.072
2019 Feb 19	04:26	3600	2.10	4585−9490	600	0.84m	3.031
2019 Feb 26	03:57	4500	2.10	4585−9490	600	0.84m	3.388
2019 Mar 06	03:48	3600	2.10	4585−9490	600	0.84m	3.860
2019 Mar 19	03:11	3600	2.10	4585−9490	600	0.84m	3.832
2019 Mar 30	03:18	3600	2.10	4585−9490	600	0.84m	3.439

Table 3. Infrared photometry of VES 263.

UT	J	H	K_s
2018 Dec 31.567	9.23 ±0.03	8.68 ±0.02	8.26 ±0.03
2019 Feb 14.045	8.75 ±0.03	8.24 ±0.04	7.87 ±0.04
2019 Fev 22.917	8.76 ±0.03	8.23 ±0.02	7.86 ±0.03

Table 4. B-band magnitude of VES 263 estimated on photographic plates taken with astrographs in Crimea (C) and Sonneberg (S). The JD column lists the geocentric JD - 2400000 (a small portion is shown here to provide guidance about its content: the full table is available in electronic form only).

JD	B	tel.
42306.437	14.82	S
42362.223	14.74	C
42630.500	14.82	S
42633.534	14.75	S
43040.477	14.66	C
43050.399	14.71	C

Ashok 2012) using the Near-Infrared Camera/Spectrograph equipped with a 1024×1024 HgCdTe Hawaii 1 array.

In photometry, the camera provides an unvignetted 8×8 square arcmin field-of-view. Frames in each filter were obtained in five dithered positions offset typically by 30 arcsec, with 5 frames being obtained in each dithered position. The corrected science frames were again median combined to produce a sky frame which was subtracted from the individual science frames. Flat field correction was applied using a sky flat derived from dark subtracted raw frames. Finally, the frames were corrected for bad pixels and cosmic ray hits. The final corrected science frames were co-added to produce an average frame on which aper-

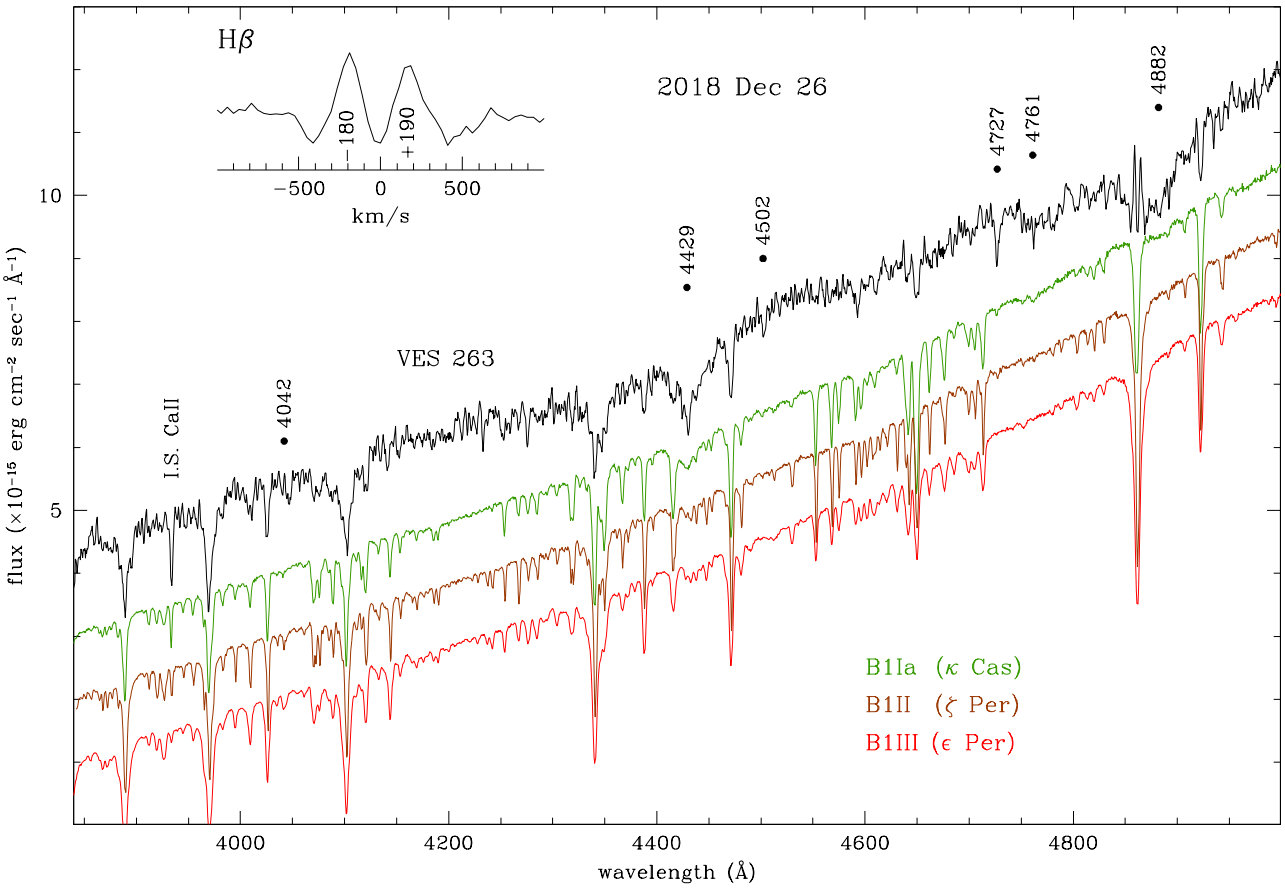

Figure 5. Medium resolution spectrum (0.60 Å/pix) of VES 263 for 2018 Dec 26 compared to those of MKK standard stars observed with the same instrumental set-up. The standards have been scaled to the same flux and slope of VES 263 and have offsets applied for plot clarity. The inset shows the velocity profile of the Hβ double-peaked emission of VES 263. Dots mark the strongest diffuse insterstellar bands.

ture photometry was done using routines in IRAF with the 2MASS field stars J20314618+4041107, J20321252+4039474 and J20320263+4035518 used for photometric calibration. The recorded JHKs photometry of VES 263 is given in Table 3.

A near-IR spectrum of VES 263 was obtained on 2019 December 31.603 UT at an airmass ∼2.7, covering the wavelength range 0.90 to 1.78μm and at a resolution R∼1000. The star was dithered to two positions along the slit to allow for sky and dark subtraction. These sky-subtracted images were used to extract 1D spectra. Wavelength calibration, accurate to a 1σ value of 0.0002 μm, was done using a combination of OH airglow lines and telluric lines that register with the stellar spectra. To remove telluric lines and to correct for instrumental response function, the target spectra were ratioed with the spectral standard SAO 71278 (Sp. type A0V, Teff = 9750 K), from whose spectra the hydrogen Paschen and Brackett absorption lines had been removed. The blackbody curve corresponding to the effective temperature of the spectral standard star was finally multiplied with the ratioed spectra. Data reduction and analysis was done using IRAF tasks and Python routines developed by us.

2.4 Objective prism plates

Six deep 103a-F photographic plates, exposed through a 4.°5 objective prism (650 Å/mm at Hγ) on various nights of November 1973, were found in the plate archive of the Asiago 67/92cm Schmidt telescope covering the sky around VES 263. Eye inspection through a high quality binocular Zeiss microscope revealed Hα to be in strong emission in VES 263 at that time. The underlying continuum appears very red and the contrast of the Hα emission is compatible with a photographic rendition of the CCD spectrum shown in Figure 4.

3 THE 2018-19 ERUPTION

3.1 Photometric behaviour

Our *BVRI* photometric monitoring of the 2018-19 eruption of VES 263, triggered by the Gaia-18azl alert, is presented in Figure 1. The behaviour is very smooth (no noticeable short time-scale changes), with the amplitude of variation growing with increasing wavelength, from ΔB=0.31 mag to ΔI=0.50 mag.

During the current 2018-19 eruption, VES 263 is redder than in the preceding quiescence, and the variability within the eruption is characterized by redder colors when the star

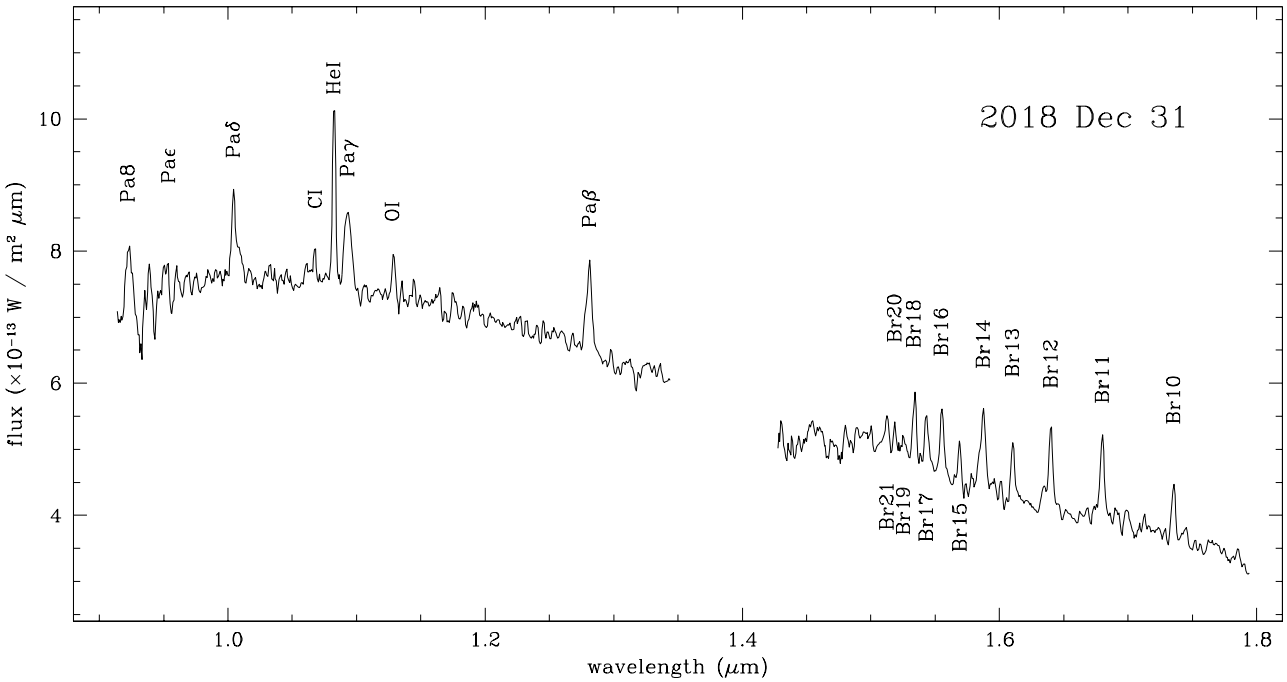

Figure 6. Near-IR spectrum of VES 263 for 2018 Dec 31 covering the Y, J, and H band wavelength range. The strongest emission lines are identified.

is brighter and bluer when fainter, in a tight correlation. This color behaviour precludes either a variable dust obscuration or a change in photospheric temperature affecting the B1II star as the causes of the observed variability. An increase in photospheric temperature would in fact make VES 263 brighter but also bluer over the whole λ-range. Similarly a reduction in the amount of dust extinction, if any should occur, would result in a brighter VES 263, but again in bluer colors.

To put the data for 2018-19 eruption into perspective, we have retrieved patrol data from the ASASSN archive (Shappee et al. 2014, Kochanek et al. 2017) and use them in Figure 2 to built a longer baseline 2014-2019 V-band lightcurve for VES 263. The ASASSN V-filter photometry is derived differentially with respect to field stars, and no color-transformation to the standard V-band is performed (M. Pawlak private communication). This may be relatively inconsequential for stars of neutral colors, but it leads to appreciable offsets for very blue or very red objects. Comparing APASS and ASASSN photometry for VES 263 in quiescence, it is obvious how the ASASSN V-filter data needs the application of a -0.048 mag offset to be brought into agreement with proper V-band magnitudes. The same offset is obtained when comparing ASASSN and our data for the current outburst. Therefore a -0.048 offset is applied to the ASASSN data before plotting them in Figure 2. The formal internal error of ASASSN data ranges from 0.011 to 0.067, with a median value of 0.015 mag.

The 2014-2017 part of the lightcurve in Figure 2 shows VES 263 stable at V=13.15, with small-amplitude and short-lived brightenings by ΔV 0.1/0.2 mag. The following three brightenings, starting with the one noticed by Gaia at the beginning of 2018, are larger in amplitude and characterized by the distinctive feature that at minima the system remains brighter than in quiescence. As illustrated by the bar at the bottom of Figure 2, the time-interval between successive brightenings steeply decreases from 217 to 138 days. This precludes them being caused by changing orbital aspect in a binary system or by rotation of a heavily spotted photosphere.

The steep decrease in the time-interval between successive brightenings also argues against them being caused by radial pulsations, in spite of the shape of the lightcurve in Figure 1 reminiscent of Cepheid variables (and similarly for RR Lyr and Mira types). Pulsating variable are known to change in amplitude and period, but much more gradually and by smaller amounts (e.g. Sterken & Jaschek 1997). However, common to all types of radial pulsators is the fact that their colors get *bluer* on the rise in brightness, while VES 263 instead turns redder. Furthermore, VES 263 lies far away from the radial pulsation instability strip on the HR diagram (see sect.7 below), and the types of non-radial pulsating variables observed around its position on the HR diagram (i.e. 53 Per, α Cyg, β Cep) are characterized by (much) shorter periods and smaller amplitudes (as documented in the *General Catalog of Variable Stars* by Samus' et al. 2017).

In this section we have been able to exclude various possible causes for the variability and current eruption displayed by VES 263 viz. variable dust obscuration, temperature changes, pulsations, stellar rotation and orbital motion. The agent responsible for the observed variability seems therefore distinct from the B1II star, something appreciably cooler, and of a large size in order to match its radiation output. In the following we'll argue this is caused by a circumstellar disk.

3.2 Long term evolution from historic photographic plates

No variability of VES 263 was noted before the recent Gaia trigger and the ASASSN patrol data, in spite of the convenient sky location and apparent brightness of the object. The obvious question thus concerns how unique is the present eruption in the context of the recorded history of the object. To investigate its past photometric behaviour, we turned our attention to the photographic plate stacks at Harvard, Moscow and Sonneberg. The earliest plate imaging VES 263 that was found in them is from 1896, the latest was exposed in 1995, thus encompassing a whole century of the object's history.

With the assistance of Edward Los of the Harvard College Observatory we accessed, prior to public release, the results of DASCH scans (Grindlay et al. 2012) of Harvard plates imaging the region containing VES 263. After culling the large number of untrustable plates, we found a total of 206 reliable DASCH measurements of VES 263 on Harvard plates which are plotted in Figure 3. Two of us (S.Y.S. and R.J.-S.) have directly accessed the plate archives of the Sternberg Astronomical Institute (SAI) in Moscow and of the Astronomical Observatory in Sonneberg (Germany) and looked for plates imaging VES 263. A total of 155 good blue-sensitive plates were found and measured (82 from the SAI 40cm astrograph, and 73 from various Sonneberg astrographs). The results are given in Table 4 and included in Figure 3. The agreement between Harvard, Moscow and Sonneberg plates is excellent in view of the limitations inherent in photographic plates and object variability. The three sets are complementary, with the Harvard plates covering the earlier years better, while the Moscow and Sonneberg plates extend to more recent epochs, and in particular filling-in the so-called Menzel's gap (1955-1965) that affected the Harvard sky patrol. The formal error of the photographic plate measurements ranges from 0.05 to 0.2 mag (median value 0.1 mag), while the dispersion of the individual datapoints along the mean lightcurve in Figure 3 is σ=0.11 mag.

The photometric behaviour in Figure 3 suggests VES 263 to have lingered around the quiescence B-band level (B=14.93 according to APASS) until about 1945 when the star begun a slow rise from $B\sim$15.05 reaching $B\sim$14.15 by $\sim$1953. It then remained around $B\sim$14.10 until about 1969 when it begun a descent reaching $B\sim$14.85 around 1972. This was followed by a resumption in brightness increase peaking at $B\sim$14.60 by 1984 and a new descent to $B\sim$14.85 by the time of the last photographic images exposed in 1995, with a trend suggesting a return to quiescence level by $\sim$1998.

The average $B\sim$14.10 level during the 1953-1969 *plateau* is far brighter than the $B\sim$14.65 value reached at the peak of the current 2018-19 outburst. For amplitude and duration, the 1953-1969 plateau is the largest event in the recorded photometric history of VES 263. On the other hand the rise to it has been slow and gradual, and the present 2018-19 eruption could be the start of a new activity cycle similar to that leading to the plateau of half a century ago.

For completeness we report that in the Sternberg plate archive in Moscow we found a further 32 plates going just deep enough to have barely recorded VES 263. These blue-sensitive plates were exposed between 1896 and 1947 with two smaller astrographs located in Moscow, with lenses 10 and 16 cm in diameter. On these plates VES 263 is seen close to the faint limit of the plates, which precludes an accurate measurement of its brightness. Nonetheless, these plates are useful to show that VES 263 was always close to quiescence brightness during this whole period, and thus excluding any major brightening like the one recorded during the 1953-1969 plateau.

3.3 Spectroscopic behaviour

A sample of the low resolution optical spectra that were acquired for VES 263 during the 2018-29 eruption are presented in Figure 4 corresponding to minimum, maximum and mid brightness. The very red slope of the continuum is obvious as is the presence of a strong Hα line in emission as also the signatures of insterstellar absorption (atomic lines and DIBs). Some HeI lines are seen in weak emission, 5876 and 7065 Å being the strongest.

A medium resolution optical spectrum of VES 263 in eruption is presented in Figure 5, focusing on the classical 3850−5000 Å interval used for spectral classification. CP12 rated their B1II classification (performed over the same 3850−5000 Å interval) as having an uncertainty negligible in the spectral type (0.5 subtypes) and larger (2 classes) in luminosity class. Consequently, in Figure 5 we compare our spectrum of VES 263 with that of template stars for spectral types B1III, B1II and B1I, selected from the Yamashita & Nariai (1977) list of recommended standards. They have been observed the same night with the same telescope and instrumental configuration as used for VES 263. For an easier comparison, their slopes have been forced to replicate that of the much more reddened VES 263, and have offsets added for plot clarity. The most significant insterstellar atomic lines and DIBs are marked.

An immediate difference with the spectrum presented by CP12 (their Figure 2) concerns the Hβ line. The CP12 spectrum was obtained in quiescence and presents a Hβ in full absorption, while the eruption spectrum in Figure 5 is characterized by a filled-in Hβ with a double-peaked emission profile which is plotted on a velocity scale in the insert. In addition, the fine details of the absorption lines appear different from CP12. The redder the continuum becomes, the less pronounced are the absorption lines, as if they are veiled by continuum emission from a cooler source. This is quite obvious when comparing the intensity of HeI 4026 with that of HeI 4922 in VES 263 and in the template stars. The appearance of HeI 4922 is significantly weakened in VES 263, while HeI 4026 stands much closer to the intensity displayed in the template stars. The putative cooler source, whose emission veils weaker lines from the B1II central star, seems also to add broader wings to the Balmer lines. Such broad wings are absent in the spectra of the template stars and also in the quiescence spectrum shown by CP12 (even if the limited resolution of their plot could lead to a wrong impression here).

Just five days past the medium-resolution optical spectrum presented in Figure 5, we have obtained the Infrared spectrum shown in Figure 6 and covering the Y, J, and H wavelength intervals. There is no trace of the B1II photospheric absorption lines, the spectrum being dominated by the continuum emission from the cooler source responsible

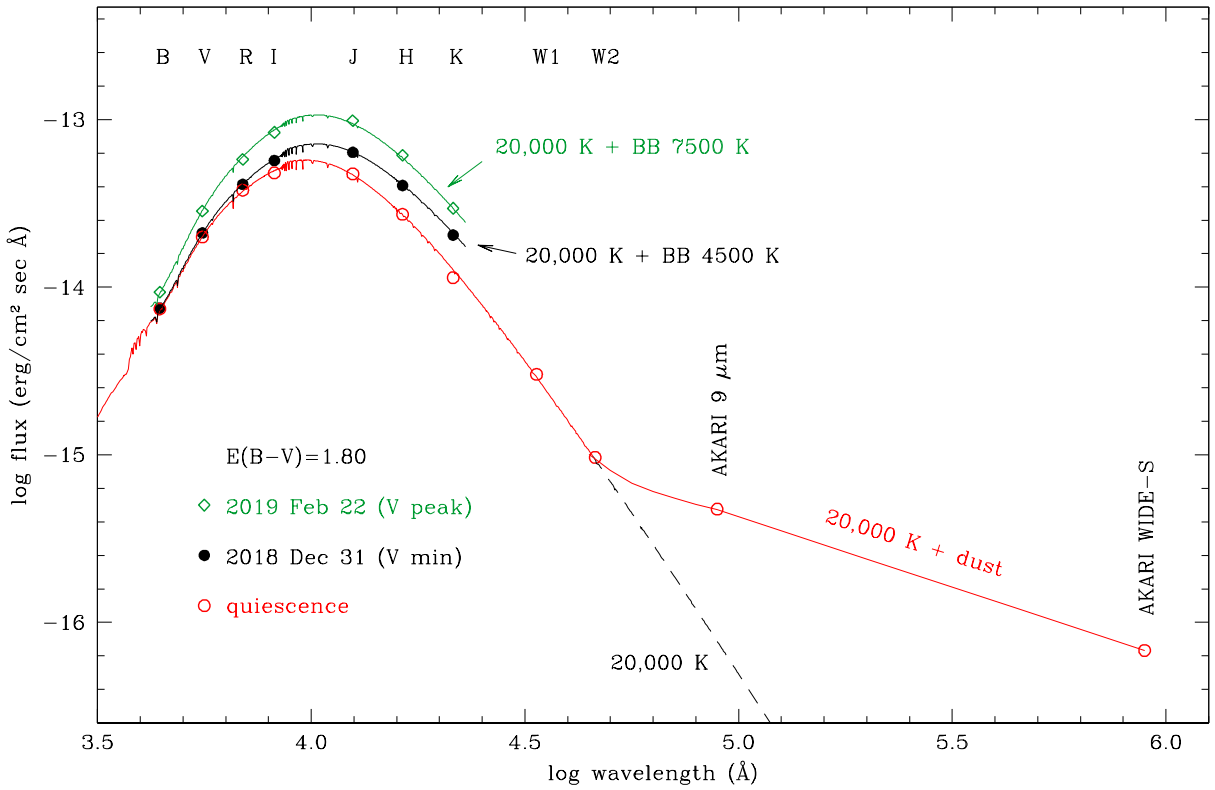

Figure 7. The spectral energy distribution of VES 263 at three distinct states (quiescence, and minimum and peak brightness during the current eruption). The SED in quiescence is fitted with a synthetic spectrum for the B1II star and black-body emission over 400−25 K for the dust. Blackbodies are added to the B1II star for the other epochs (all reddened by the same E_{B-V}=1.80).

for the photometric eruption. The Paschen and Brackett series of hydrogen appear in emission as also a fairly strong HeI 1.083 μm feature. Weaker features at 1.0686 and 1.1287 μm are attributed to CI and OI. Since the OI 1.1287 μm line is significantly strengthened by Lyman continuum fluorescence (Mathew et al. 2018) and it is seen here in emission whereas the continuum fluoresced OI 1.3164 μm is not,it implies the presence of a copious source of LyC photons whose source must obviously be the hot B1II central star. Comparing the slope of the optical spectra in Figure 4 rising toward the red, with that of the Infrared spectrum in Figure 6 going the opposite way, it's evident how the peak of VES 263 observed spectral energy distribution is placed around 1.0 μm.

It is also worth noting that the Brackett lines in the H-band are optically thick because Br10 at 1.7362 μm is weaker than the higher Brackett lines like Br11, Br12 etc. whereas it would be expected to be stronger had Case B conditions been followed for emission coming from an optically thin gas. That the HI lines are optically thick is not a surprise, since as shown in coming sections, the object is identified as a HAeBe star with a disk and the disk in such stars, from which the HI lines originate, are expected to have high densities of 10^{11} to 10^{13} cm^{-3} (Mathew et al. 2018, and references within). At such high densities the Brackett hydrogen lines are expected to be optically thick (Hummer & Storey 1987; Storey & Hummer 1995)

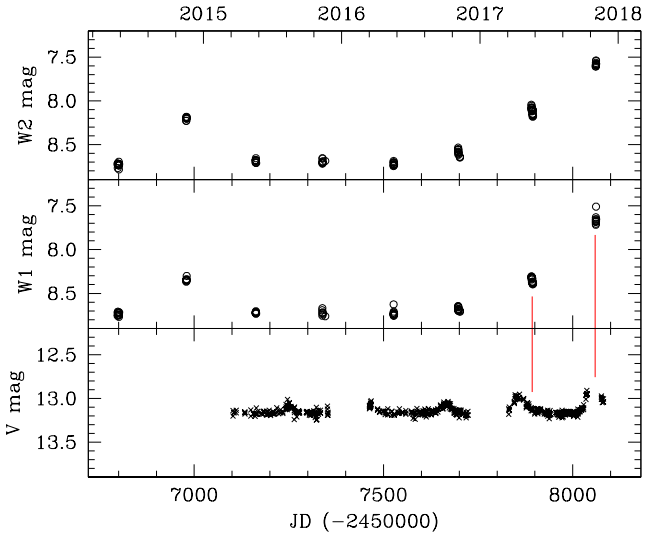

Figure 8. Comparison between NeoWISE data and V-band photometry of VES 263. The lines are meant to guide the eye.

4 THE SPECTRAL ENERGY DISTRIBUTION

The spectral energy distribution of VES 263 is presented in Figure 7. Three epochs are considered: those of minimum and maximum in brightness during the current 2018-19 eruption, and the phase of preceeding quiescence.

The spectral energy distribution (SED) in quiescence is built from 2009-2014 multi-epoch APASS optical pho-

tometry (reporting average values as B=14.93, V=13.15, R=12.11, and I=11.22), 2MASS JHK_s data for 1998 (Cutri et al. 2003), AKARI S9W,WIDE-S measurements for 2006-2007 (Ishihara, et al. 2010; Ali-Lagoa et al. 2017), and AllWISE[1] W1,W2 data for 2010 (Cutri et al. 2013). Such data are obviously non-simultaneous, but since the object was in a quiescent state during this time, it should result in any significant difference.

The calibrations of the MK spectral types in terms of photospheric temperature, summarized by Tokunaga (2000) and Drilling & Landolt (2000), average to 20,000 K for B1 giant/supergiants. To fit the energy distribution for VES 263 in quiescence in Figure 7, we have selected from the grid computed by Castelli and Kurucz (2003) the synthetic spectrum appropriate for a B1II star (parameters: $T_{\rm eff}$=20,000 K, [M/H]=0.0 and $\log g$=3.0), and adopted the Fitzpatrick (1999) extinction law for the standard R_V=3.1 case. The excellent fit in Figure 7 is obtained for E_{B-V}=1.80. A similar good fit and reddening would be obtained adopting a blackbody distribution for T=20,000 K. Both fitting with a synthetic spectrum or with a blackbody are not over-sensitive to temperature: considering that the optical-IR is located on the Rayleigh-Jeans tail of the energy distribution for stars as hot as the B1II in VES 263, the actual temperature makes a small difference (fits with 19,000 or 21,000 K blackbodies or synthetic spectra would perform equally good in Figure 7), and the shape of the observed SED is actually controlled by the reddening, with a change by ΔE_{B-V}=±0.05 being readily appreciable.

The SED in quiescence shows a large excess over the 20,000 K photospheric emission for $\lambda \gtrsim 6$ μm. The IR-excess in Figure 7 is fitted by adding black-body emission from dust distributed in temperature from 400 to 25 K. The presence of warm circumstellar dust is a distinctive feature of HAeBe stars (eg. Stahler & Palla 2005). The luminosity radiated by such dust is $L_{\rm IR}$∼12 $L_\odot$. It was obtained by integrating the (unreddened) flux in excess of the 20,000 K photospheric synthetic spectrum in Figure 7, and scaling it to the distance of VES 263 (sect. 6).

The SED of VES 263 at minimum and peak brightness during the 2018-19 eruption are plotted in Figure 7 using our simultaneous $BVRI$ and JHK observations for 2018 Dec 31 and 2019 Feb 22, respectively. A good fit to the SED at minimum is obtained by adding a 4500 K blackbody to the synthetic spectrum for the B1II star. The SED at maximum is instead fitted by adding a 7500 K blackbody to the emission from the B1II central star (both 4500 K and 7500 K blackbodies being reddened by the same E_{B-V}=1.80 affecting the 20,000 K synthetic spectrum). Such 4500 K and 7500 K blackbodies have, respectively, λ-integrated luminosities of 120 and 860 $L_\odot$. This fitting exercise shows that the brightness and colors during the eruption of VES 263 are governed by the presence and variability of a source both cooler and separate/additional to the central B1II star, that we identify with the circumstellar disk (see sect.8 below) that is a typical feature of pre-Main Sequence objects (Stahler & Palla 2005). The surface temperature of a disk obviously depends on the distance from the central star, and therefore the 4500 K and 7500 K values found above are to be interpreted as averages weighted over the respective surfaces emitting at $BVRI$ and JHK wavelengths.

It is worth noticing that the minor brightenings visible in the pre-eruption lightcurve of Figure 2, are also linked to the variable presence of a source much cooler than the stellar photosphere (i.e. the disk). This can be easily inferred from Figure 8, where the NeoWISE data (Mainzer et al. 2011, 2014) available for VES 263 are plotted in phase with the V-band lightcurve. It is evident how (1) during quiescence the NeoWISE $W1$ and $W2$ data (Nugent et al. 2015) stay flat and close to the AllWISE $W1$=8.58 and $W2$=8.50 mag values characterizing the quiescent SED of Figure 7, and (2) any minimal brightening visible in the V-band reverberates into a much larger increase at NeoWISE $W1$ and $W2$ wavelengths. The AllWISE catalog combines observations from the 2009-2010 cryogenic and post-cryogenic survey phases of the NASA Wide-field Infrared Survey Explorer (WISE), and NeoWISE refers to the data the satellite is collecting since it has been brought out of hibernation and resumed observation in 2014.

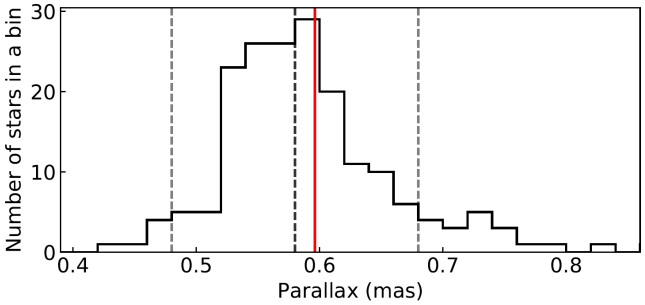

Figure 9. Distribution of *Gaia* DR2 parallax measurements of confirmed members of the Cyg OB2 association. The parallax of VES 263 is marked with the red vertical solid line. Black vertical dotted lines indicate our parallax selection, centred at 0.58 mas, that was used to study the proper motion of the association.

5 ASTROMETRIC MEMBERSHIP TO THE CYG OB2 ASSOCIATION

Analysis of *Gaia* astrometry supports VES 263 being a member of the Cyg OB2 association. To this aim, we started by acquiring a list of hot OB stars in this association compiled by Wright, Drew & Mohr-Smith (2015) and in an extended region around the densest part of the association by CP12 and Berlanas et al. (2018). As their membership designation is historically mainly attributed by over-density of spectroscopically confirmed OB stars in that region (Ivanov 1996), we first queried *Gaia* DR2 data (Gaia Collaboration et al. 2018) in a cone with the radius of 1° centered at α = 308.163° δ = 41.299° and matched the *Gaia* observations with previously determined members. Already confirmed by Berlanas et al. (2019), the members are concentrated around parallax ∼0.58 mas with a possible extension to closer distances. VES 263, marked with a solid vertical line in Figure 9, is located close to the peak of that distribution.

Having more than 800,000 stars, that could smear out

[1] We ignore AllWISE W3,W4 data because of conflicting results reported for PSF-fitting and aperture photometry measurements, and their large scatter depending on the radius of aperture.

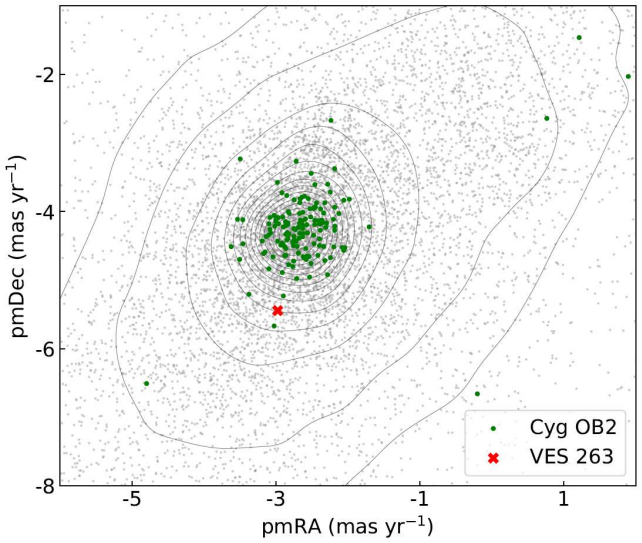

Figure 10. Distribution of selected stars in proper motion space, with indicated association members and VES 263. The density profile, shown as equidistant contours, was created by summing 2D Gaussian probability density function (PDF) of all stars. PDFs were defined by stellar proper motion and its reported uncertainty.

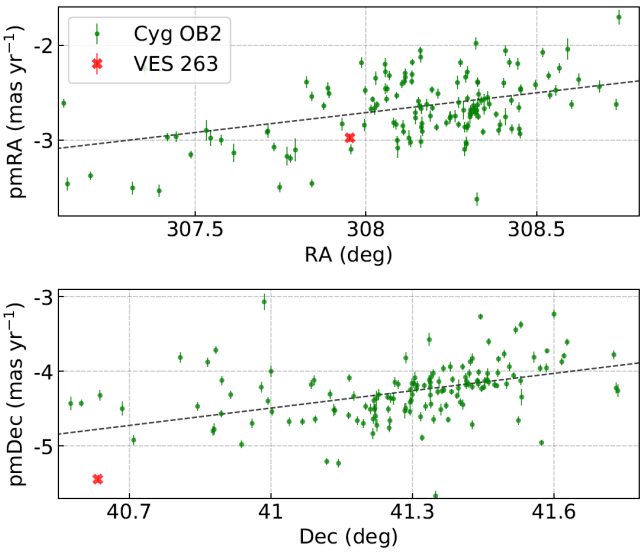

Figure 11. Distribution of proper motion and sky location of the Cyg OB2 members and VES 263 in the right ascension (*top*) and declination (*bottom*) planes.

over-densities of few hundreds of stars in the proper motion space, we limited our selection to stars with a parallax measurement between 0.48 and 0.68 mas (also indicated in Figure 9). This selection resulted in 11561 stars of which 153 are members of the association, together plotted in Figure 10. The same figure shows over-density of stars with the same proper motion as known Cyg OB2 members. If we move our selection to higher/lower parallax values the over-density disappears. VES 263 falls on the outskirt of this peak, where the density of stars in proper motion space starts to increase. Disregarding the clear velocity outliers, that might not be part of the association, VES 263 has a velocity consistent with other members. As the OB associations are proven not to be bound (Mel'nik & Dambis 2017; Wright 2018) and have larger physical sizes than open clusters with considerable small-scale kinematics substructure (Wright 2018), a greater velocity scatter is expected for them. As VES 263 is not located in the main part of the association, but in its extended region, its velocity vector might indicate radial expansion. Plots in Figure 11 show dependency of members' proper motion on their position in the sky. Both plots show some trends, where VES 263 is consistent with the scatter along the fitted line and therefore membership to Cyg OB2.

From fitting to isochrones Wright et al. (2015) concluded that the majority of star formation in Cyg OB2 occurred more or less continuously between 1 and 7 Myr ago, which should then bracket the age of VES 263. At an estimated total mass of ∼16,500 $M_\odot$, Cyg OB2 is one of the most massive groups of young stars known in our Galaxy.

6 DISTANCE AND INTERSTELLAR REDDENING

The Gaia DR2 parallax for VES 263 is 0.5962 mas, with an error of just ±0.0253 (4%) that allows a safe direct inversion (Gaia Collaboration et al. 2018) to derive the distance as ∼1.68±0.07 kpc. At a Galactic latitude of only +0.60 deg, the sightline accumulates a lot of interstellar reddening upon reaching VES 263, as already clear from the SED fitting of the previous section requiring E_{B-V}=1.80±0.05.

There are several 3D maps of interstellar extinction that may be employed to derive estimates of the reddening affecting VES 263. Stilism by Lallement et al. (2014) and Capitanio et al. (2017) provides E_{B-V}=1.98±0.25, and the 3D Pan-STARRS1 map by Green et al. (2018) returns E_{B-V}=2.06±0.21. An appreciable lower error is associated to the IPHAS 3D map by Sale et al. (2014) giving an extinction A_V=6.19, with lower and upper limits at A_V=5.85 and A_V=6.55 combining IPHAS and Gaia uncertainties. For the R_V=3.1 extinction law, using the quadratic expression of Fiorucci and Munari (2003) for early B-type stars suffering from high reddening, this translates to E_{B-V}=1.92 with formal lower and upper limits of E_{B-V}=1.82 and E_{B-V}=2.03.

At such high reddening, the interstellar NaI lines are too strong (core saturated) in our Echelle spectra of VES 263 to allow using them to derive the reddening, as illustrated in Figure 12. Interstellar KI lines are however still far from saturation. The equivalent width 0.410±0.006 Å that we have measured for KI 7699 Å on our Echelle and medium resolution spectra (cf. Figure 12) translates into E_{B-V}=1.76±0.03 following the calibration by Munari and Zwitter (1997).

The diffuse interstellar bands (DIBs) do present a general trend to get stronger with increasing reddening (e.g. Jenniskens & Desert 1994), but the correlation is far from being a tight or unique one. Our Echelle spectra of VES 263 have recorded a rich sample of DIBs, a few being shown in Figure 12. Two sightline categories, named ζ and σ, have been described by Krelowski et al. (1992) and Krelowski & Sneden (1994) which correspond to *UV-shielded* and *non-shielded* sightlines, probing cloud cores and external regions, respectively. Vos et al. (2011) show that there are fundamental differences between the two groups in correlations

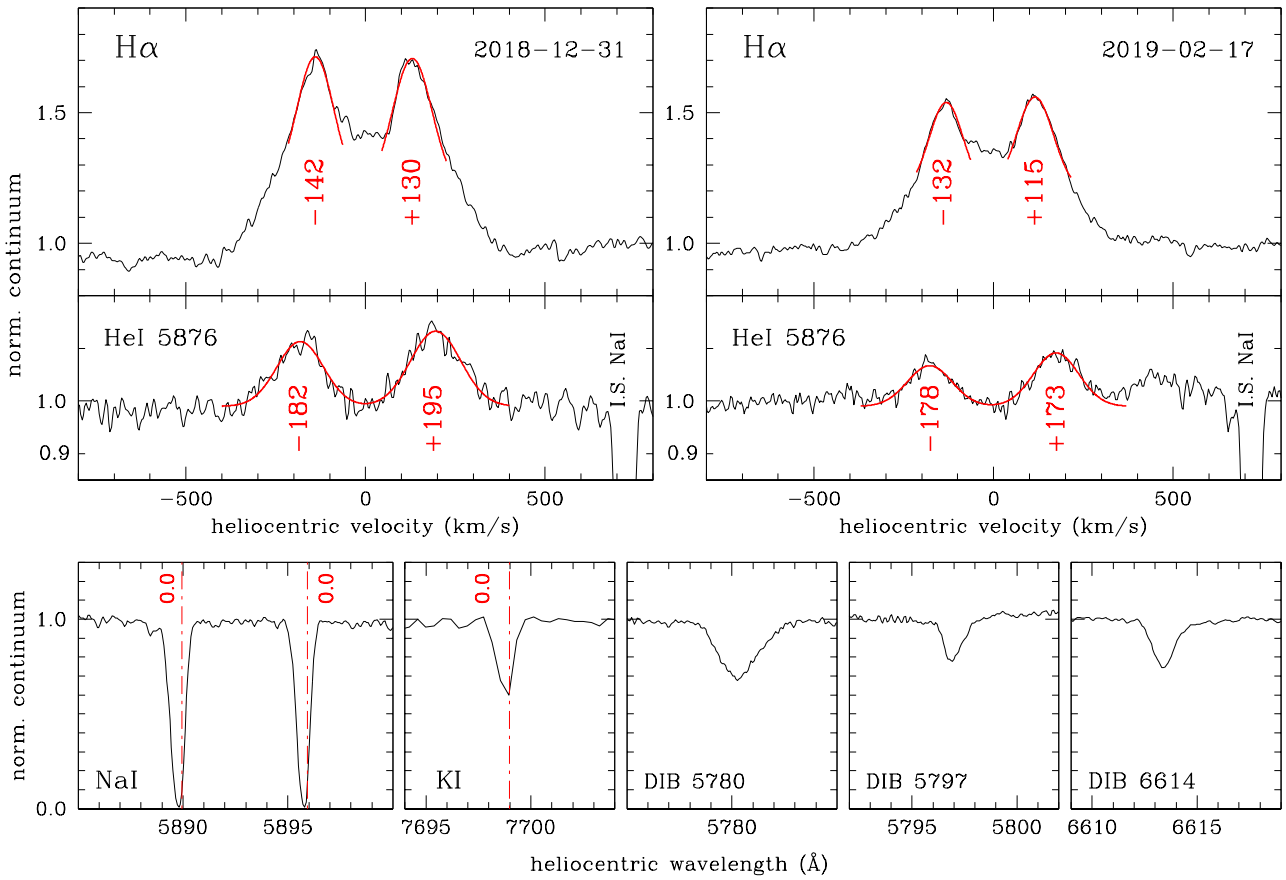

Figure 12. *Top*: Gaussian fitting to the double-peaked line profiles of Hα and HeI 5876 for minimum (left) and maximum (right) brightness during the 2018-19 eruption. *Bottom*: interstellar lines and DIBs as recorded on the Asiago Echelle spectra. The dash-dotted lines mark null heliocentric radial velocity.

Table 5. Summary of results from reddening indicators. E.W. is the equivalent width of the interstellar spectral feature and E_{B-V} the corresponding reddening as derived from the published relations discussed in sect. 6.

	E.W.(Å)	err	E_{B-V}	err
DIB 5705	0.1372	0.0036	1.23	0.03
DIB 5797	0.2264	0.0014	1.23	0.01
DIB 5850	0.1018	0.0015	1.20	0.02
DIB 6379	0.1389	0.0022	1.18	0.02
		mean:	1.21	0.02
DIB 5780	0.7592	0.0081	1.40	0.02
DIB 6196	0.0787	0.0070	1.41	0.11
DIB 6270	0.1527	0.0067	1.44	0.06
DIB 6614	0.3511	0.0081	1.43	0.03
		mean:	1.42	0.03
Pan-STARRS 1			2.06	0.21
Stilism			1.98	0.25
KI 7699	0.4096	0.006	1.76	0.03
B1II SED			1.80	0.05
IPHAS 3D			1.92	0.12
		adopted:	1.80	0.05

between DIBs, reddening, and gas. The two sightline categories are named after those toward ζ Oph and σ Sco. Kos and Zwitter (2013) found that DIBs at 5705, 5780, 6196, 6202, and 6270 Å do not show much difference between ζ and σ sightlines, while DIBs at 4964, 5797, 5850, 6090, 6379, and 6660 Å have distinctly different relations for ζ and σ sightlines between their equivalent width and E_{B-V} reddening. The ratio of the equivalent width (EW) of DIBs 5780 and 5797 allows to distinguish between the two types of sightlines: an $EW_{5797}/EW_{5780}>0.3$ corresponds to ζ category, and conversely an $EW_{5797}/EW_{5780}<0.3$ to σ category. The DIBs at 5780 and 5797 Å in our Echelle spectra of VES 263 are shown in Figure 12. Their equivalent widths are 0.755 and 0.330 Å respectively, corresponding to ζ-type sightline categories. In Table 5 we report our measurement of the equivalent width of the DIBs best visible in our Echelle spectra of VES 263, and the corresponding reddening E_{B-V} derived by applying the ζ-type calibration given by Kos and Zwitter (2013). Such reddenings tightly cluster around two distinct values, $E_{B-V}=1.21\pm0.02$ and $E_{B-V}=1.42\pm0.03$. Such values are mutually incompatible and also far too small compared to all other indicators summarized in Table 5. Other E.W./E_{B-V} calibrations for DIBs (e.g. Munari 2014) result in values similar to those of Table 5, and therefore we conclude that DIBs along the sightline to VES 263 do not conform to published reddening relations calibrated over large portions of the sky.

The three most accurate reddening determinations among those summarized in Table 5 come from KI 7699, SED fitting and IPHAS 3D map, for an average value of E_{B-V}=1.80±0.05 that we will adopt in the rest of this paper.

7 ABSOLUTE MAGNITUDE AND THE HR DIAGRAM

From the Gaia DR2 parallax, E_{B-V}=1.80 reddening and APASS V=13.15, the absolute magnitude of VES 263 in quiescence is M_V=−3.75 mag. This is equivalent to a bolometric magnitude M_{bol}=−5.64 mag adopting from Flower (1996) a bolometric correction B.C.=−1.89 for giants/supergiants with T_{eff}=20,000 K, and M_{bol}^{Sun}=+4.74 (Bessell, Castelli & Plez 1998; Torres 2010). The corresponding luminosity is L=14,000 $L_\odot$, which is close to L=12,000 $L_\odot$ as obtained by direct flux integration of the (unreddened) synthetic T_{eff}=20,000 K spectrum in Figure 7.

The position on the HR diagram of HAeBe stars as catalogued by Vioque et al. (2018) is shown in Figure 13. The position and error bars for VES 263 correspond to L=13,000±3,000 $L_\odot$ and T_{eff}=20,000±2,000 K. The corresponding blackbody radius would be 9.5±1.2 $R_\odot$. In the same figure we have plotted the pre-Main Sequence tracks for three values of the mass from Bressan et al. (2012), leading to an estimate of ≈12 M$_\odot$ for VES 263.

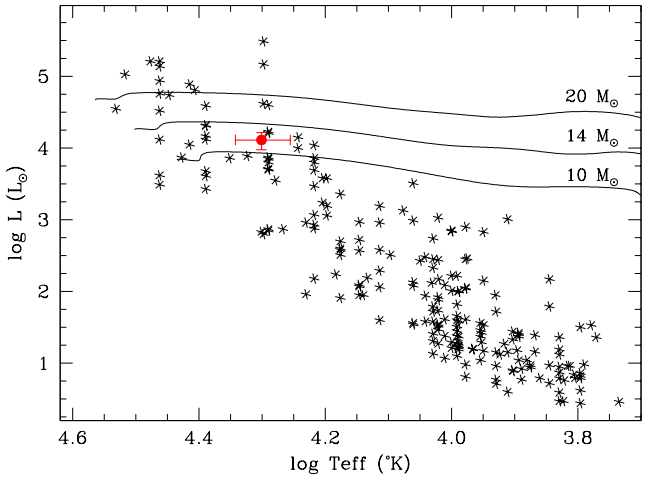

Figure 13. The position of VES 263 on the HR diagram. The asterisks mark data for the HAeBe stars in the compilation by Vioque et al. (2018). The lines are pre-Main Sequence evolutionary tracks from Bressan et al. (2012).

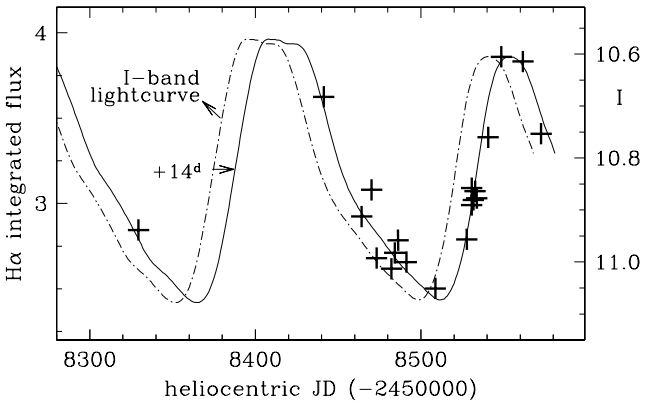

Figure 14. Evolution with time of the integrated flux of Hα emission line of VES 263, from data in Table 2. The dot-dashed line is the I-band lightcurve from Figure 1, the same shifted by 14 days is plotted as the continuous line.

8 THE ACCRETION DISK

8.1 Evidence from emission line profiles

The emission profile for Hα and HeI 5876 in VES 263 at the time of maximum and minimum brightness during the 2018-19 eruption are plotted in Figure 12. Such double-peaked profiles are typical of circumstellar disks (Horne & Marsh 1986). The origin in a disk is reinforced noting that the peaks of HeI lines have a larger velocity separation than Hα. The excitation potential for HeI 5876 is ∼23 eV, twice larger than the ∼12 eV for Hα, and population of the upper level for HeI 5876 requires hotter and denser regions compared to Hα, which means an inner disk radius and therefore a faster Keplerian rotation. The ratio of velocity separation of the double-peaked Hα:HeI 5876 profiles goes like 1.0:1.4 for VES 263, which quite favorably compares with the average value 1.0:1.5 we have measured for a sample of quiescent cataclysmic variables (CVs) we have observed over the years with the same Asiago Echelle spectrograph used to observe VES 263. In CVs, the emission lines are well known to form in the accretion disk around the central white dwarf (e.g. Warner 1995).

From line fitting in Figure 12, the projected rotational velocity of the disk at the location of Hα formation is $v \sin i$∼130 km s^{-1}. Assuming a pure Keplerian rotation for the disk and adopting from the previous section 12 M$_\odot$ and 9.5±1.2 $R_\odot$ for the central star, the Hα forms at ≈14 stellar radii for an inclination of the disk i=90° and ≈7 stellar radii for i=45°.

In addition to the SED distributions in Figure 7, the disk as the agent reponsible for the variability observed in 2018-19 is also supported by the evolution with time of the integrated flux of Hα, which is listed in Table 2 and plotted in Figure 14. The Hα behaviour in Figure 14 matches exactly the lightcurve of VES 263. For the latter we selected the I-band brightness because its effective wavelength is the closest to the peak of the energy distribution of VES 263 (cf. Figure 7). The ΔI=0.50 mag amplitude of the lightcurve translates into a change of the photometric flux by 58%, which is the same as the 54% change in the integrated flux of Hα as listed in Table 2.

A noteworthy feature in Figure 14 is the ∼14 days shift between Hα and the I-band. The brightness of the disk is proportional to the mass-flow through it (Ichikawa & Osaki, 1992). Similarly, the integrated flux of Hα traces the mass-flow through the inner regions of the disk where the temperature is high enough to excite the emission from the line. The ∼14 days delay appears therefore to be the average time required for mass to migrate from the outer regions of the disk where the bulk of the emission in the I-band originates to the inner regions where the temperature is hot enough to excite emission from Hα.

A final remark on the disk is offered by Figure 12. Close to minimum brightness (Dec 2018 spectrum) the velocity separation of the double-peaked line profiles is larger than at maximum brightness (Feb 2019 spectrum). A higher brightness corresponds to a larger mass flow through the disk, and therefore a given temperature is reached at an outer radius (given the classical $T_{\rm eff} \propto M_{\rm acc}^{1/4}$ dependence). The temperature required to excite emission from Hα is then reached at a greater distance from the central star, resulting in a lower Keplerian velocity and consequently a reduced velocity separation of the double-peaked line profile (similarly for HeI 5876). Precisely what is seen in Figure 12.

8.2 Looking for orbital motion

The high resolution Echelle spectroscopic observations of VES 263 listed in Table 2 cover a time interval of about 200 days. Photospheric absorption lines are veiled by featureless continuum emission by the disk, leaving only the Hα emission line to derive the radial velocity. A sample of the recorded Hα profiles is presented in Figure 15.

Many massive stars are found in binary systems, as it is the case for the majority of O- and B-type stars in open clusters and OB associations (e.g. Boeche et al. 2004), with mass ratios closer to $q \sim$1 than less massive binaries. Their orbital periods can be as short as 1-2 days with consequently orbital velocities of hundreds of km s^{-1}. The line photocenter in Figure 15 is stable around the average value of $RV_{\odot}$=$-$4.1$\pm$0.9 km s^{-1}. The dispersion of measurement (σ=2.5 km s^{-1}) is similar to the dispersion of intra-night individual spectra, suggesting minimal or null change in radial velocity during the monitored 200 days. This leads to basically three different explanations: (1) the B1II star is single, or any companion is far less massive ($q \ll$1), (2) the orbital period is much longer than the sampled 200 days, or (3) the orbital inclination is very low (face-on orientation). The latter explanation is the less probable, because it is reasonable to assume that in a binary the circumstellar disk lies close to the orbital plane, and the disk in VES 263 has a considerable inclination given the large velocity separation of the peaks in the emission line profiles (Figure 12). Alternatives 1 and 2 could either be true, as their combination. To further investigate them, we plan to continue gathering high resolution spectra of VES 263 in the future.

In addition to keeping their photocenter stable, the line profiles in Figure 15 do not change their shape other than reducing the velocity separation in response to changes in the mass flow through the disk. This indicates that over the 200 days of monitoring the inner regions of the disk where Hα forms remained circular and symmetric, excluding precession of an asymmetric shape for the disk.

8.3 Mass accretion rate

Mass accretion ($M_{\rm acc}$) and accretion luminosity ($L_{\rm acc}$) are related by

$$L_{\rm acc} = G\frac{M_* M_{\rm acc}}{R_*} \qquad (1)$$

where M_* and R_* are the mass and radius of the accreting object, respectively. This can be used to obtain an order-of-magnitude estimate of the mass flow rate through the disk of VES 263 and onto its central star.

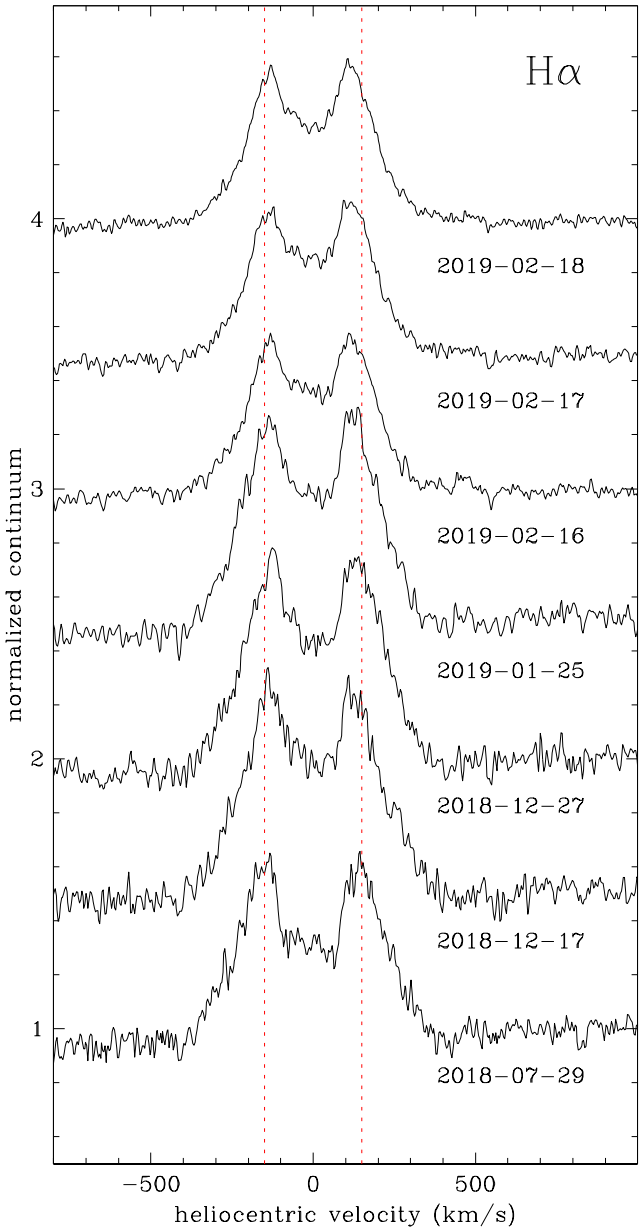

Figure 15. Comparison of the Hα emission profile of VES 263 as observed at different epochs with the Asiago 1.82m + Echelle spectrograph (adjacent continuum normalized to 1.0). The lines at $-$150 and +150 km s^{-1} are plotted to guide the eye.

The SED of VES 263 at maximum and minimum brightness during the current 2018-19 eruption is characterized by excess radiation at optical and near-IR wavelengths that, when fitted with blackbodies and their emission integrated over the whole wavelength range, provides luminosities of 860 and 120 L$_{\odot}$, respectively (cf. Figure 7 and sect.4). The corresponding mass accretion rates would be 1.12$\times$10^{-5} and 1.43$\times$10^{-6} M$_{\odot}$ yr^{-1}. They are however lower limits to the actual value of $M_{\rm acc}$, because the fit with blackbodies of $T_{\rm eff}$=7,500 and 4,500 K miss the emission from the inner and hotter regions of the disk able to sustain the formation of Balmer and HeI emission lines. To access them it would

be essential to gather satellite observations in the ultraviolet, difficult to obtain in view of the very large excintion affecting VES 263 (of the order of 15 mag at 2000 Å).

To test the hypothesis that the accretion luminosities derived in the previous paragraph are lower limits, we may estimate $L_{\rm acc}$ from the reddening-corrected observed flux ($F_{\rm line}$) of emission lines, following a common practice for pre-Main Sequence objects. The isotropically radiated luminosity $L_{\rm line}$ in the given line is related to distance d through

$$L_{\rm line} = 4\pi d^2 F_{\rm line} \quad (2)$$

The transformation of $L_{\rm line}$ into $L_{\rm acc}$ is usually obtained by power-law relations of the type

$$\log(\frac{L_{\rm acc}}{L_\odot}) = A_{\rm line} + B_{\rm line} \times \log(\frac{L_{\rm line}}{L_\odot}) \quad (3)$$

with calibrations of $A_{\rm line}$,$B_{\rm line}$ coefficients existing for many emission lines. Integrating the flux of emission lines visible in the near-IR spectrum of Figure 6 and adopting their $A_{\rm line}$,$B_{\rm line}$ coefficients from Fairlamb et al. (2017) leads to accretion luminosities ranging from 200 to 1300 $L_\odot$, with a median value of 900 $L_\odot$. This confirms as a lower limit the 120 $L_\odot$ accretion luminosity derived above from integration of SED for the same date (2018 Dec 31), the time of minimum during the current 2018-19 eruption. It would have been interesting to repeat the exercise with a similar near-IR spectrum taken during a maximum in the current 2018-19 eruption, but unfortunately we have none. We do have however in Table 2 an extended series of flux measurements for the Hα emission line. Adopting the corresponding $A_{\rm line}$,$B_{\rm line}$ coefficients from Mendigutía et al. (2011), the derived accretion luminosities range from 280 to 450 $L_\odot$. The amount of reddening correction to Hα is however vastly larger than for the near-IR emission lines, and uncertainties on E_{B-V} could easily account for part of the 2× difference in their respective $L_{\rm acc}$.

The accretion luminosity $L_{\rm acc}$ has also been found to correlate with the luminosity of the central star $L_\star$. The analysis of existing data by Mendigutía et al. (2015), shows that for HAeBe the accretion luminosity ranges from $L_{\rm acc}$∼$L_\star$ to 0.01 $L_\star$. VES 263 follows this rule with – from data above – $L_{\rm acc}$∼0.07×$L_\star$ at minimum and $L_{\rm acc}$∼0.5×$L_\star$ at maximum of the current 2018-19 eruption.

Finally, it appears worth noticing that the recent calibration by Arun et al. (2019) of $M_{\rm acc}$ as funtion of the mass of the central star in HAeBe objects predicts $M_{\rm acc}$≈3.3×10^{-5} $M_\odot$ yr^{-1} for a 12 $M_\odot$ star as in VES 263. This well compares with the lower limit $M_{\rm acc}$⩾1.1×10^{-5} $M_\odot$ yr^{-1} estimated in this section for the accretion rate at the peak of the present VES 263 eruption.

8.4 Wind and jets

The low resolution spectra listed in Table 2 show a low-level variability in the immediate vicinity of Hα emission line. They are compared in Figure 16. To avoid confusion with the many DIBs present in the region, the principal ones are identified in the top-panel of the figure. Three numbers are given for each DIB, namely the FWHM (in Å), the equivalent width (in Å, scaled to that of DIB 6614), and the wavelength of the photocenter (in Å), averaging among the

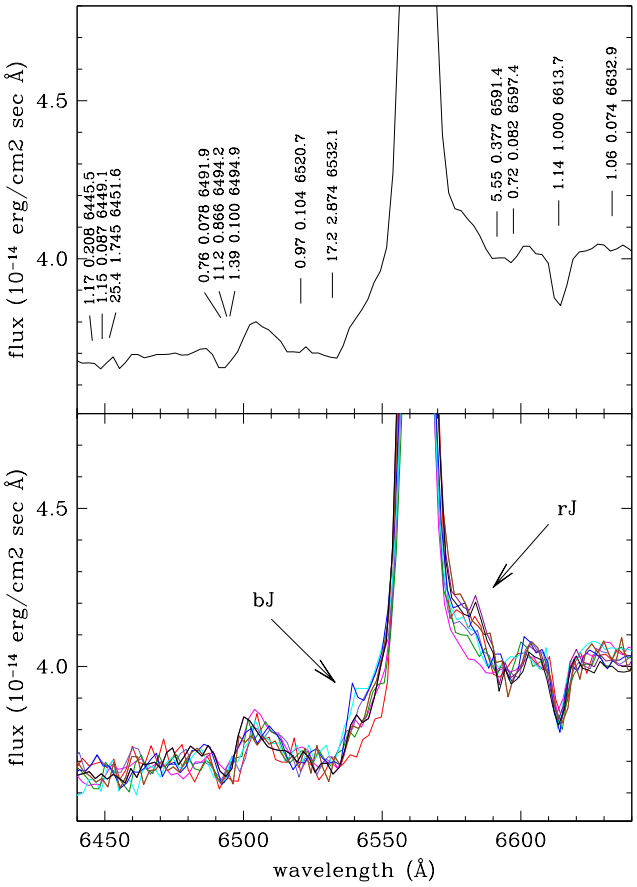

Figure 16. *Top panel:* Average around Hα of the low-res spectra of VES 263. The strongest DIBs in the compilation by Jenniskens & Desert (1994) are marked (see sect. 8.4 for associated numbers). *Bottom panel:* the individual spectra making up the above average are plotted individually (after matching their median value). The arrows point to regions at ≈ −700 and +700 km s^{-1} where the dispersion is larger (see sect. 7.4).

values reported by Jenniskens & Desert (1994) in their surveys of DIBs toward several hot stars. Figure 16 shows that indeed the dispersion of individual spectra is larger in the immediate vicinity of Hα.

A variable *hump* is present in emission to the red of Hα, at a bulk velocity of ≈ +700 km s^{-1}. Symmetrically placed at a bulk velocity of ≈ −700 km s^{-1} there is a variable absorption, or as an alternative a variable second emission hump. To distinguish between these two alternatives for the blue feature is not easy in view of the limited spectral resolution and S/N of the spectra in Figure 16. To complicate the matter is the deep depression of the stellar continuum caused by the nearby very strong DIB 6532. Devoted observations, at higher S/N and greater spectral dispersion, are required to properly address the issue, which we plan to perform in the future. These features are relatively minor, carrying a flux ∼1/10 of that of the main Hα line. They are barely at the threshold of detection in Echelle observations, being lost in the strong curvature imposed by the instrumental blaze function at the center of the order, where Hα is situated.

We propose the features at +700 km s^{-1} and −700 km s^{-1} to be the signature of possible bipolar jet ejection

from the central regions of the accretion disk surrounding the central star. That at -700 km s^{-1} could appear in absorption instead of emission if seen projected onto the central B1II star or the brightest inner regions of the disk. The escape velocity from the central star is $\sim$700 km s^{-1} (assuming R=9.5 R$_\odot$ and M=12 M$_\odot$). The similarity of the jet velocity and the escape velocity is a general property of all objects known to posses collimated mass-outflows (Livio 1997). Bipolar jets have been observed in many HAeBes (Stahler & Palla 2005), sometimes extending to such great distances from the central star to be easily resolved spatially by ground-based observations (e.g. Günther, Schneider, & Li, 2013; Melnikov et al. 2008; Grady et al., 2004; Corcoran & Ray, 1998).

9 CONCLUSIONS

The observational evidence discussed in previous sections proves the variable presence of a massive accretion disk in VES 263. The SED in Figure 7 shows how the contribution of such a disk was negligible when the object was in quiescence, and become dominant at redder wavelengths during the current 2018-19 eruption. Furthermore, the strict parallel behavior between disk brightness and integrated Hα flux shown in Figure 14 proves how the ups-and-downs in the lightcurve are correlated to the variable mass-flow through the disk.

What causes such a variability in the mass being fed to the disk is unknown, and its investigation is beyond the scope of the present paper. It is however intriguing to note from Figures 1 and 2 how the photometric activity and mean brightness have been increasing on the average during the last few years, signalling a gradual resumption of mass-feeding and flow through the disk. This behavior seems parallel to the slow and contrasting rise ($\sim$8 yrs) from quiescence to peak brightness at the time of the large eruption of the 1950's, illustrated in Figure 3. It is tempting to argue that the 1950's eruption was caused by a similar resumption of the accretion disk as we are witnessing now. If the current event should turn into a replica of the eruption of the 1950's, then we are at present only just half-way to its peak brightness.

VES 263 is clearly worth a continuing detailed, multi-wavelength monitoring over the coming years, as well as a dedicated effort to locate further information about its colorful past history.

10 ACKNOWLEDGEMENTS

We are grateful to the anonymous referee for valuable comments that helped to improve the paper. We acknowledge Jonathan Grindlay and Edward Los of Harvard College Observatory for their permission to use DASCH data on VES 263 prior to inclusion in public DR6 scheduled for 2019. R.J.S. thanks the team of Sonneberg Observatory and 4pi Systeme company for hospitality and Peter Kroll and Eberhard Splittgerber for help and permission to use the historical plate archive. The research work at the Physical Research Laboratory is funded by the Department of Space, Government of India. S.Y.S. is supported by Grant VEGA No 2/0008/17 and Development Program from M.V. Lomonosov Moscow State University ('Physics of stars, relativistic objects and galaxies'). K.Č. acknowledges financial support of the Slovenian Research Agency (research core funding No. P1-0188 and project N1-0040). R.J.-Š. is supported by University of Rijeka under the project number uniri-prirod-18-3. The observations presented in this paper have been collected in part with ANS Collaboration telescopes, the Galileo 1.22m telescope of the University of Padova, and the INAF Copernico 1.82m and Schmidt 67/92cm telescopes.

REFERENCES

Alí-Lagoa V., Müller T. G., Usui F., Hasegawa S., 2018, A&A, 612, A85
Arun R., et al., 2019, AJ, 157, 159
Banerjee D. P. K., Ashok N. M., 2012, BASI, 40, 243
Berlanas S. R., Herrero A., Comerón F., Pasquali A., Bertelli Motta C., Sota A., 2018, A&A, 612, A50
Berlanas S. R., Wright N. J., Herrero A., Drew J. E., Lennon D. J., 2019, MNRAS, 484, 1838
Bessell M. S., Castelli F., Plez B., 1998, A&A, 333, 231
Boeche C., Munari U., Tomasella L., Barbon R., 2004, A&A, 415, 145
Bressan A., Marigo P., Girardi L., Salasnich B., Dal Cero C., Rubele S., Nanni A., 2012, MNRAS, 427, 127
Capitanio L., Lallement R., Vergely J. L., Elyajouri M., Monreal-Ibero A., 2017, A&A, 606, A65
Castelli F., Kurucz R. L., 2003, IAUS, 210, A20
Comerón F., Pasquali A., 2012, A&A, 543, A101 (CP12)
Corcoran M., Ray T. P., 1998, A&A, 336, 535
Cutri R. M., et al., 2003, yCat, 2246,
Cutri R. M., et al., 2013, yCat, 2328
Downes R. A., Keyes C. D., 1988, AJ, 96, 777
Drilling J. S., Landolt, A. U., 2000, in Allen's Astrophysical Quantities, 4th ed., Arthur N. Cox. editor, AIP Press (New York), p.381
Fairlamb J. R., Oudmaijer R. D., Mendigutia I., Ilee J. D., van den Ancker M. E., 2017, MNRAS, 464, 4721
Fiorucci M., Munari U., 2003, A&A, 401, 781
Fitzpatrick E. L., 1999, PASP, 111, 63
Flower P. J., 1996, ApJ, 469, 355
Gaia Collaboration, et al., 2018, A&A, 616, A1
Grady C. A., et al., 2004, AIPC, 713, 47
Green G. M., et al., 2018, MNRAS, 478, 651
Grindlay J., Tang S., Los E., Servillat M., 2012, IAUS, 285, 29
Günther H. M., Schneider P. C., Li Z.-Y., 2013, A&A, 552, A142
Henden A., Munari U., 2014, CoSka, 43, 518
Herbig G. H., 1960, ApJS, 4, 337
Horne K., Marsh T. R., 1986, MNRAS, 218, 761
Hummer D. G., Storey P. J., 1987, MNRAS, 224, 801
Ichikawa S., Osaki Y., 1992, PASJ, 44, 15
Ishihara D., et al., 2010, A&A, 514, A1
Ivanov G. R., 1996, A&AT, 9, 305
Jenniskens P., Desert F.-X., 1994, A&AS, 106, 39
Kochanek C. S., et al., 2017, PASP, 129, 104502
Kohoutek L., Wehmeyer R., 1997, AAHam, 11,
Kohoutek L., Wehmeyer R., 1999, A&AS, 134, 255

Kos J., Zwitter T., 2013, ApJ, 774, 72
Krelowski J., Sneden C., 1994, ASPC...58, 12, ASPC...58
Krelowski J., Snow T. P., Seab C. G., Papaj J., 1992, MNRAS, 258, 693
Lallement R., Vergely J.-L., Valette B., Puspitarini L., Eyer L., Casagrande L., 2014, A&A, 561, A91
Livio M., 1997, IAU Colloq. 163: Accretion Phenomena and Related Outflows, 845, ASPC..121
Lynds B. T., 1962, ApJS, 7, 1
Mainzer A., et al., 2011, ApJ, 731, 53
Mainzer A., et al., 2014, ApJ, 792, 30
Mathew B., et al., 2018, ApJ, 857, 30
Mel'nik A. M., Dambis A. K., 2017, MNRAS, 472, 3887
Melnikov S., Woitas J., Eislöffel J., Bacciotti F., Locatelli U., Ray T. P., 2008, A&A, 483, 199
Mendigutía I., Calvet N., Montesinos B., Mora A., Muzerolle J., Eiroa C., Oudmaijer R. D., Merín B., 2011, A&A, 535, A99
Mendigutía I., Oudmaijer R. D., Rigliaco E., Fairlamb J. R., Calvet N., Muzerolle J., Cunningham N., Lumsden S. L., 2015, MNRAS, 452, 2837
Munari U., et al., 2012, BaltA, 21, 13
Munari U., Henden A., Frigo A., Dallaporta S., 2014, JAD, 20
Munari U., Moretti S., 2012, BaltA, 21, 22
Munari U., 2014, ASPC, 490, 183
Munari U., Zwitter T., 1997, A&A, 318, 269
Nugent C. R., et al., 2015, ApJ, 814, 117
Sale S. E., et al., 2014, MNRAS, 443, 2907
Samus' N. N., Kazarovets E. V., Durlevich O. V., Kireeva N. N., Pastukhova E. N., 2017, ARep, 61, 80
Shappee B. J., et al., 2014, ApJ, 788, 48
Stahler S. W., Palla F., 2005, The Formation of Stars, Wiley-VCH
Stephenson C. B., Sanduleak N., 1977, ApJS, 33, 459
Sterken C., Jaschek C., 1996, Light Curves of Variable Stars, Cambridge Univ. Press
Storey P. J., Hummer D. G., 1995, MNRAS, 272, 41
Tokunaga A. T., 2000, in Allen's Astrophysical Quantities, 4th ed., Arthur N. Cox. editor, AIP Press (New York), p.143
Torres G., 2010, AJ, 140, 1158
Vioque M., Oudmaijer R. D., Baines D., Mendigutía I., Pérez-Martínez R., 2018, A&A, 620, A128
Vos D. A. I., Cox N. L. J., Kaper L., Spaans M., Ehrenfreund P., 2011, A&A, 533, A129
Warner B., 1995, Cataclysmic Variable Stars, Cambridge Astrophysical Series, vol. 28, Cambridge Univ. Press
Wisniewski W., Coyne G. V., 1976, VatOP, 1, 225
Wright N. J., Drew J. E., Mohr-Smith M., 2015, MNRAS, 449, 741
Wright N. J., 2018, Cambridge Workshop on Cool Stars, Stellar Systems, and the Sun, pag. 75
Yamashita Y., Nariai K., 1977, An Atlas of Representative Stellar Spectra, University of Tokyo Press